ORIGINAL PAPER

Check for
updates

Micromechanical analysis of hydraulic fracturing in the toughness-dominated regime: implications to supercritical carbon dioxide fracturing

Mengli Li[1,2] · Fengshou Zhang[2] (iD) · Li Zhuang[3] · Xi Zhang[4] · Pathegama Ranjith[5]

Abstract

Supercritical carbon dioxide (SC-CO$_2$) is considered as an ideal non-aqueous fracturing fluid due to its superior properties of liquid-like density, gas-like viscosity, high compressibility, and diffusivity. This study aims to investigate the micromechanical behavior of SC-CO$_2$ fracturing in both intact and fractured rock samples by using a coupled fluid-solid discrete element method (DEM) model. A new numerical algorithm for hydraulic fracturing in the toughness-dominated regime is developed by assuming that the pressure in the whole fracture is uniform. This new numerical algorithm could achieve a much higher computational efficiency compared with the conventional hydromechanical scheme in DEM. Hydraulic fracturing cases using high-viscosity fracturing fluid are also performed for comparison. The results indicate that the fracture propagation induced by SC-CO$_2$ tends to be less smooth and continuous, more asymmetric, and tortuous compared to that induced by viscous fluid. Besides, the low-viscosity fluid like SC-CO$_2$ can lead to a lower breakdown pressure, and the fluid leak-off into the rock matrix can result in a lower breakdown pressure and higher fracture propagation pressure. The simulations also illustrate that SC-CO$_2$ fracturing tends to create a more complex and productive fracture network if the pre-existing natural fractures are involved. As a result, we can conclude that SC-CO$_2$ could be an alternative fracturing fluid to induce a more effective fracture network for hydrocarbon production.

Keywords Hydraulic fracturing · Supercritical carbon dioxide · DEM · Toughness-dominated · Tortuosity · Breakdown pressure

1 Introduction

Hydraulic fracturing has become a widespread reservoir stimulation technique for hydrocarbon production from low-permeability formations. However, conventional hydraulic fracturing with water-based fracturing fluid has some disadvantages, including environmental impacts caused by the flow-back water and the high cost of water usage. Furthermore, since gas productivity is greatly dependent on the water sensitivity of shale gas formations, water-based fracturing is not suitable for the water-sensitive clay-abundant formations [1–4]. There is an urgent requirement to explore the feasibility of non-aqueous fracturing technologies to overcome these drawbacks. Supercritical carbon dioxide (SC-CO$_2$) has been considered as an ideal non-aqueous fracturing fluid due to its superior properties of liquid-like density, gas-like viscosity, high compressibility, and diffusivity [1]. Furthermore, the use of SC-CO$_2$ could make shale a major host for the geological carbon storage [5, 6]. In recent years, despite astounding progress made in understanding the mechanics of hydraulic fracturing following the boom of unconventional resource development, the mechanism of SC-CO$_2$ fracturing has not been fully understood yet.

✉ Fengshou Zhang
fengshou.zhang@tongji.edu.cn

1 State Key Laboratory of Shale Oil and Gas Enrichment Mechanisms and Effective Development, Beijing 100083, China

2 Department of Geotechnical Engineering, Tongji University, Shanghai 200092, China

3 Extreme Engineering Research Center, Korea Institute of Civil Engineering and Building Technology, Goyang, Gyeonggi 10223, Republic of Korea

4 CSIRO Energy, Melbourne, Australia

5 Department of Civil Engineering, Monash University, Clayton, Victoria 3800, Australia

Hydraulic fracture is known to have complex multiscale behavior. The fracturing behavior is determined by the interplay of two energy dissipation mechanisms (viscosity and toughness) and two fluid storage mechanisms (storage and leak-off) [7]. These two sets of competing mechanism are associated with four limiting regimes: storage viscosity [8], storage toughness [9], leak-off viscosity [10], and leak-off toughness [11]. Conventional hydraulic fracturing with water-based fracturing fluid usually approaches or even falls into the viscosity-dominated regime due to the relatively large viscosity of fracturing fluid, if the leak-off is not dominant. In such a regime, the energy is mainly dissipated by the viscous fluid flow inside the fracture, while the energy expended in fracturing solid medium is negligibly small. There is a gradual transition to the toughness-dominated regime with the decrease of fracturing fluid viscosity. Thus, the fracture propagation driven by SC-CO_2 likely corresponds to the toughness-dominated regime because of its gas-like viscosity [12]. Both the fracture profiles and pressure response can be vastly different among different hydraulic fracture propagation regimes [13–15].

Hydraulic fracture initiation and propagation are mainly affected by some key factors including rock properties, confining pressure, pressurization rate, and fluid type [16–21]. Experimental studies of hydraulic fracturing were carried out to investigate the fracturing behavior for different types of fluid. Besides the fluid viscosity, recent analyses showed that the composition and state of the fracturing fluid also play important roles [22, 23]. Ishida et al. [24–26] conducted experiments using oil, water, liquid CO_2 (L-CO_2), and SC-CO_2 to fracture granite. It was observed that SC-CO_2 fracturing leads to the lowest breakdown pressure, the highest tortuosity [27], and the most complex fracture network with many secondary branches due to the reduced viscosity and enhanced infiltration. A possible explanation can be that the low-viscosity fracturing fluid like SC-CO_2 could easily penetrate into defects in the rock and subsequently cause more fractures. The fracturing experiments in non-bedded sandstone using different viscous fracturing fluids showed similar results [28]. In addition, it is necessary for hydraulic fracture to activate and connect pre-existing natural fractures to generate a large fracture network [29, 30]. The growth behavior of SC-CO_2-induced fractures in layered shale [28, 31, 32] and bedded sandstone [33] was explored in laboratory experiments. The results suggest that SC-CO_2 promotes the fracture complexity with secondary branches by activating microfractures. More shear-dominant fractures were also observed along the grain boundaries inclined in the direction of the maximum compressive stress when using low-viscosity fracturing fluid [26, 27]. The key parameters for SC-CO_2-related hydraulic fracturing experiments in the literature are summarized in Table 1. Those experimental studies showed some macroscale fracturing behavior induced by SC-CO_2, but the fracture growth behavior induced by SC-CO_2 in the naturally fractured rock needs further exploration and the micromechanical analysis to reveal the mechanism in depth is still lacking.

Numerical simulation is a powerful tool to reproduce the fracturing process and help to understand the mechanism of

Table 1 Summary of the key parameters for SC-CO_2-related hydraulic fracturing experiments in the literature

Sample	Size (mm)	Fracturing fluid	Fracturing characteristics	Reference
Granite	Cubic, 190	Viscous oil → Water	More wavelike, branched, and thinner fractures	[24]
Granite	Cubic, 170	L-CO_2 → SC-CO_2	More three-dimensional fractures; lower breakdown pressure	[25]
Granite	Cubic, 170	Viscous oil → Water → L-CO_2 → SC-CO_2	More three-dimensional, tortuous, and shear-dominant fractures; lower breakdown pressure	[26]
Granite	Cubic, 170	Viscous oil → Water → SC-CO_2	More tortuous, branched, and shear-dominant fractures	[27]
Shale, non-bedded sandstone	Cubic, 200	Water → L-CO_2 → SC-CO_2	More branches, more likely to connect with natural fracture and bedding; lower breakdown pressure	[28]
Shale	Cylindrical, 85/170 (D/L)	Viscous oil → Water → L-CO_2	More shear-dominant and branched fractures; larger fracture opening	[31]
Shale	Cylindrical, 100/∼ 150, 100/∼ 200 (D/L) Cubic, 300	Water → CO_2	More shear-dominant fractures; more complex networks; higher leak-off; lower breakdown pressure	[32]
Layered tight sandstone	Cubic, 300	X-linked guar → Slick water → SC-CO_2	More branches; smaller fracture opening; higher leak-off; lower breakdown pressure	[33]

hydraulic fracturing. The injection fluid properties, such as compressibility, viscosity, and interfacial tension, are the main factors investigated through numerical modeling [34–37]. Based on the cohesive zone model in conjunction with a poroelasticity model, it was found that fluid viscosity has more significant effect on the hydraulic conductivity and leak-off coefficient than fluid compressibility [34]. Moreover, fluid viscosity could influence the fluid flow behavior and the evolution of the poroelastic stress around the borehole, resulting in the low-viscosity fluid filtrating into the fractures easily [35, 37]. Meanwhile, the interfacial tension of fracturing fluid controls whether fluid invades the pore space at the borehole wall [37]. Thus, hydraulic fracturing induced by SC-CO$_2$ could be more efficient due to its high compressibility, low viscosity, and low interfacial tension, particularly for the rock containing natural microcracks [38].

In this study, we applied a fully coupled fluid-solid discrete element method (DEM) model to study the micromechanical behavior of SC-CO$_2$ hydraulic fracturing. We developed a new numerical algorithm for hydraulic fracturing in the toughness-dominated regime. The algorithm can achieve a much higher computational efficiency than the traditional hydromechanical scheme for hydraulic fracturing modeling with low fluid viscosity. Based on the numerical algorithm, the comparison between hydraulic fracturing with SC-CO$_2$ in the toughness-dominated regime and that with high-viscosity fluid approaching the viscosity-dominated regime was made.

2 Numerical algorithm of hydraulic fracturing with DEM

2.1 New algorithm for the toughness-dominated regime

The numerical modeling is carried out by employing the discrete element code PFC2D [39], in which the model is assembled by bonded circular particles [40]. The linear parallel bond model is applied to mimic the rock deformation and failure behavior at microscale [41]. The fluid-driven fracture propagation process is an emergent behavior of bonding breakage in either tensile or shear modes. Besides, there are additional joints represented by using the smooth joint model (SJM) to simulate the discontinuities in fractured rock mass [42]. The SJM can simulate the behavior of a smooth interface with user-defined macroscopic properties such as friction, cohesion, and dilation.

The fluid-solid coupling is implemented by applying a fluid network based on the porous structure formed by the particles [39, 43]. As shown in Fig. 1 a, a series of enclosed domains are created by connecting the centers of neighboring particles while the fluid pressure in a domain is applied to the surface of surrounding particles. Therefore, there is a drag force (F_{fluid}) for each particle calculated from the resultant force of surrounding domain pressure (P) (see Fig. 1b). The aperture between two particles is assumed to be a flow channel, which is initially inactivated since the sample in this study is impermeable unless mentioned. If the normal stress or the shear stress exceeds the corresponding bond strength, the bond breaks, which results in the generation of a microcrack. Then, the corresponding flow channel is activated and the fluid flow is allowed (see Fig. 1c).

The developed new algorithm for the toughness-dominated regime is shown in the flow chart in Fig. 2. In the toughness-dominated regime, the energy is mainly spent in fracturing the rock, and the energy dissipated by viscous flow is negligible. The pressure gradient along the fracture length is nearly zero. Thus, this algorithm assumes that the pressure in the whole fracture is uniform. The fluid volume inside the hydraulic fracture can be viewed as a whole, and the goal is to match the current opened fracture volume (V_c) with the injection fluid volume (V_f). The change of fluid pressure is proportional to the volume difference as given in Eq. (1). Note that the
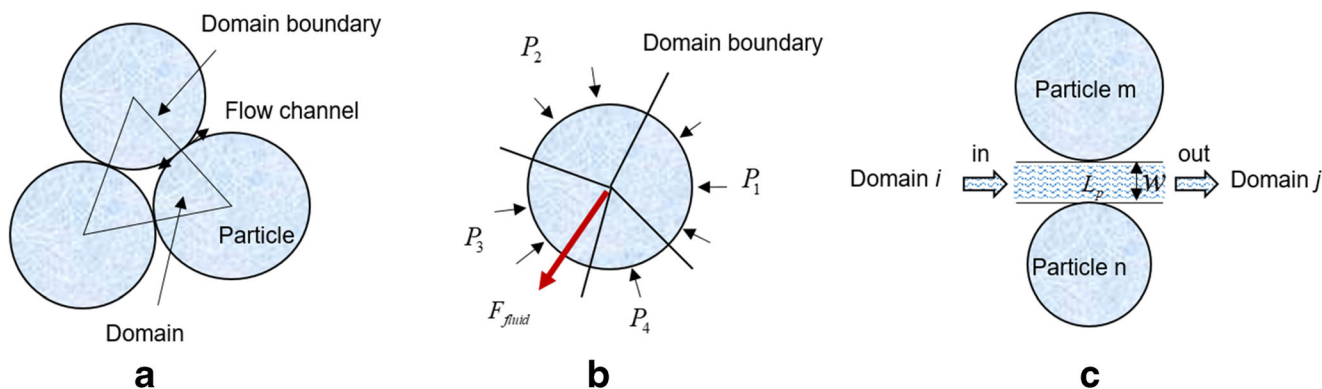

Fig. 1 Fluid flow model based on DEM (modified from [35, 43]). **a** The enclosed domain formed by the neighboring particles. **b** The drag force on a particle calculated from the pressure of surrounding domains. **c** Fluid flow in the activated channel after the corresponding bond breaks. P_1, P_2, P_3, and P_4 are the surrounding domain pressures acting on the particle, and F_{fluid} is the resultant force of P_1, P_2, P_3, and P_4

Fig. 2 Proposed numerical algorithm for the toughness-dominated regime
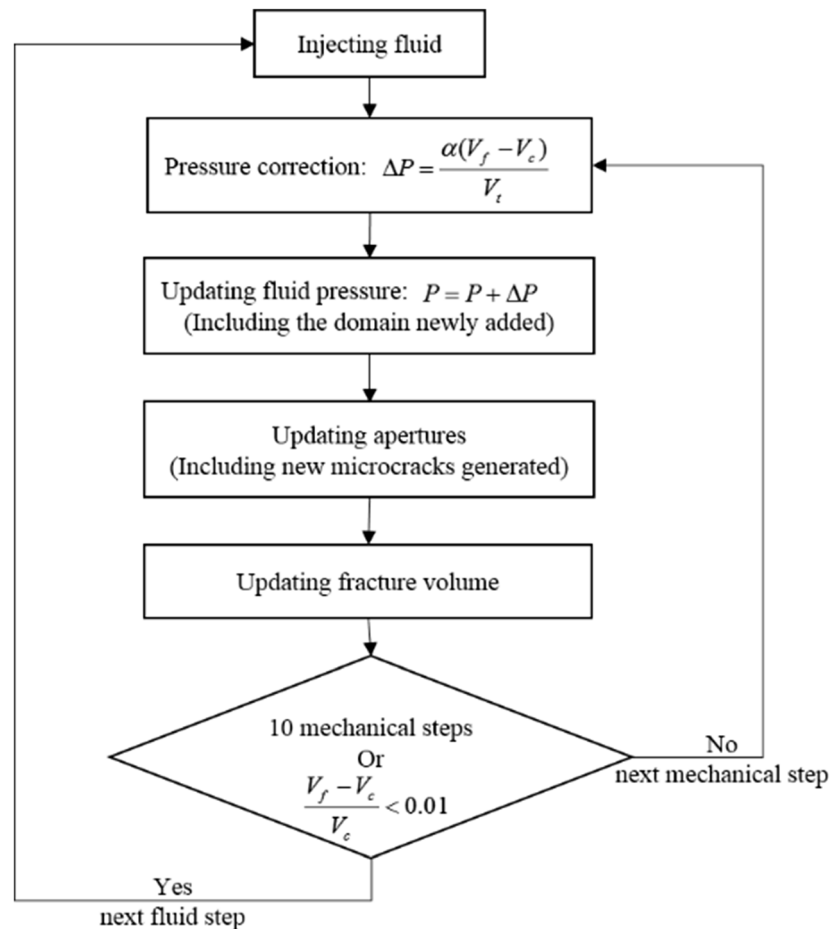
compressibility of SC-CO_2 is not considered here and the effect of compressibility is analyzed in Section 5. The fracture volume is calculated from the aperture width (w) and the length of flow channel (l_p) as shown in Eqs. (2) and (3). The apertures and current opened fracture volume are updated with the apparent fluid pressure acting on the surrounding particles. At each fluid time step, up to ten mechanical steps are executed except that the balance of the fluid volume and fracture volume is achieved (less than 1% difference).

$$\Delta P = \alpha(V_f - V_c)/V_t \tag{1}$$
$$V_c = \sum l_p(w - w_0) \tag{2}$$
$$V_t = \sum l_p w \tag{3}$$

where ΔP is the pressure increment at each mechanical time step, α is a coefficient proportional to the rock stiffness, V_t is the total fracture volume, w is the aperture width, w_0 is the assumed initial aperture width, and l_p is the length of the flow channel, which is the distance between two connecting domain centers.

2.2 Comparison with the conventional hydromechanical scheme

For the conventional hydromechanical scheme [39, 43], unequal fluid pressure accumulates in each domain as a result of pressure gradient along the fracture length. The fluid flow inside the fracture is calculated at each fluid time step (d_t), and the change of fluid pressure for each fluid domain is given by the following equation:

$$\Delta P = K_f(\sum q d_t - dV_d)/V_d \tag{4}$$

where K_f is the fluid bulk modulus, V_d is the apparent volume of the domain, dV_d is the change of domain volume per fluid time step, and $\sum q$ is the total flow rate per fluid time step in the domain. The flow rate (q) in the channel is given as a function of the aperture (w), the fluid viscosity (μ), the pressure difference (ΔP) between the two domains, and the length of flow channel (l_p)

$$q = \frac{w^3}{12\mu} \frac{\Delta P}{l_p} \tag{5}$$

For both the conventional hydromechanical scheme and the developed new algorithm for the toughness-dominated regime, the aperture width (w) is updated with contact normal force as follows:

$$\text{Compressive normal force}: w = \frac{w_0 F_0}{F + F_0} \qquad (6)$$

$$\text{Zero normal force}: w = w_0 + w_{\text{mech}} \qquad (7)$$

where w_{mech} is the gap between two particles, F is the current contact normal force, and F_0 is the normal force at which the aperture decreases to 50% of the initial aperture (w_0).

In the conventional hydromechanical scheme, since the fluid time step is proportional to the term of fluid viscosity over fracture aperture ($dt \propto \frac{\mu}{K_f w^2}$), the fluid time step could be very small for low-viscosity fluid such as SC-CO_2. In contrast, fluid viscosity and fracture aperture are irrelevant to the fluid time step for the toughness-dominated regime and it can therefore be 2 orders of magnitude larger than that for the conventional hydromechanical scheme. Consequently, a much higher computational efficiency can be achieved based on the new proposed algorithm for hydraulic fracturing in the toughness-dominated regime.

3 Numerical model setup

3.1 Model description

A two-dimensional intact rock sample (1.0 m × 1.0 m) with an injection point at the center is generated in this study. The particle radius is randomly distributed between 3 and 5 mm by using a given random seed number. The sample is subjected to two types of biaxial compressive stresses: one with 10 MPa in the x direction and 12 MPa in the y direction and the other with 10 MPa in the x direction and 15 MPa in the y direction. Young's modulus of the intact rock sample is 29.1 GPa, and Poisson's ratio is 0.30 based on the numerical simulation of unconfined compressive strength test. The uniaxial compressive strength and tensile strength of the intact rock sample are 22.3 MPa and 4.8 MPa, respectively. Through the biaxial compressive test, the intact rock friction angle and cohesion are 37.5° and 5.8 MPa, respectively. Besides the intact rock sample, a fractured rock sample which contains 18 natural fractures is also generated as shown in Fig. 3. The natural fractures obey the SJM, which allows slip and separation at particle contacts [42]. The frictional stress on the weakly bonded natural fractures is assumed to obey Coulomb's frictional law. The initial aperture is 0.1 mm, which is 17 times larger than the assumed residual aperture. The fracturing fluid is not able to invade the natural fracture until the corresponding bond breaks and connects to the hydraulic fracture. The algorithm for the toughness-dominated regime is applied to the modeling cases with SC-CO_2 (fluid viscosity 0.06 cp), while the traditional hydromechanical coupling scheme is applied to the cases with high viscosity of 100 cp. The input parameters for the numerical model and the microscale parameters for the contact models are summarized in Tables 2 and 3, respectively. Hydraulic fracturing simulation cases in both intact and fractured rock samples are listed in Table 4.

To test the accuracy of the new numerical algorithm for the toughness-dominated regime, the simulation results are compared with the reference solution for a plane strain Khristianovic-Geertsma-de Klerk (KGD) hydraulic fracture [14]. It is first necessary to determine the regime of propagation. There are four limiting regimes as shown in Fig. 4: storage viscosity (M) [8], storage toughness (K) [9], leak-off viscosity ($\widetilde{M}$) [10], and leak-off toughness ($\widetilde{K}$) [11]. The fracture propagation regimes are determined by the dimensionless
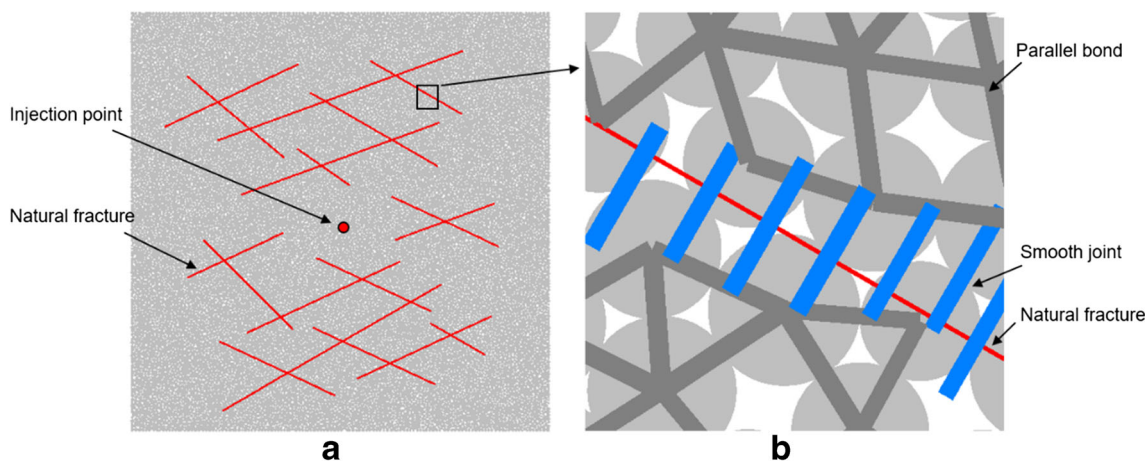

Fig. 3 Pre-existing natural fractures in rock sample. **a** 18 fractures inserted in the model sample. **b** Close-up view of one natural fracture. The red lines represent pre-existing natural fractures, and the blue and gray thick lines in **b** indicate the contact normal

Table 2 The parameters for the numerical model

Model properties	Values
Model size (m)	1.0×1.0
Number of particles	17,511
Particle radius (mm)	3–5
Particle density (kg/m^3)	3169
Compressive stress in x, S_{min} (MPa)	10
Compressive stress in y, S_{max} (MPa)	12/15
Young's modulus, E (GPa)	29.1
Poisson's ratio, v	0.30
Uniaxial compressive strength, σ_c (MPa)	22.3
Uniaxial tensile strength, σ_t (MPa)	4.8
Friction angle, φ (°)	37.5
Cohesion, c (MPa)	5.8
Bulk modulus of rock, K (GPa)	8.3
Proportionality coefficient, α (MPa)	0.2
Assumed residual aperture, w_0 (m)	$6e{-}6$
Assumed joint initial aperture, w_{0j} (m)	$1e{-}4$
Injection rate, Q (m^2/s)	$0.5e{-}4$
Injection fluid viscosity (cp)	0.06 and 100

time (τ) and the toughness parameter (K_m) as follows:

$$\tau = \frac{E' C'^6}{\mu' Q^3} t \quad (8)$$

$$K_m = \left(\frac{K'^4}{\mu' E'^3 Q} \right)^{1/4} \quad (9)$$

where Q is the fluid injection rate, t is the injection time, and μ', E', K', and C' are the material parameters defined as follows:

Table 3 The microscale parameters for the contact models

Microscale input parameters	Values
Young's modulus of the particle (GPa)	17
Ratio of stiffness of the particle	2.5
Friction coefficient of the particle, μ	0.5
Young's modulus of the parallel bond (GPa)	17
Ratio of stiffness of the parallel bond	2.5
Tensile strength of the parallel bond (MPa)	8
Cohesion of the parallel bond (MPa)	15
Friction angle of the parallel bond (°)	30
Normal stiffness of SJM (GPa/m)	120
Shear stiffness of SJM (GPa/m)	60
Tensile strength of SJM (MPa)	0.1
Cohesion of SJM (MPa)	0.1
Friction coefficient of SJM	0.5

$$\mu' = 12\mu, E' = \frac{E}{1-v}, K' = 4\left(\frac{2}{\pi}\right)^{1/2} K_{IC}, C' = 2C_L \quad (10)$$

where μ is the fluid viscosity, E is Young's modulus, v is Poisson's ratio, K_{IC} is the mode I fracture toughness of the rock, and C_L is Carter's leak-off parameter.

In this study, K_m is the decisive parameter due to the absence of leak-off. As shown in [14], the hydraulic fracture propagates in the toughness-dominated regime for $K_m > 4.80$ and in the viscosity-dominated regime for $K_m < 0.70$. When the mode I fracture toughness of the random model is 2.66 Pa·m$^{1/2}$, which is inversely calculated in the next section of this paper, the toughness parameter (K_m) calculated for the modeling cases with SC-CO$_2$ and 100 cp fluid are 6.99 and 1.09, respectively. Therefore, the fracture propagation driven by SC-CO$_2$ belongs to the toughness-dominated regime, while that induced by 100 cp fluid approaches the viscosity-dominated regime.

3.2 Model verification

In order to verify the hydraulic fracturing model in the toughness-dominated regime, simulation of hydraulic fracturing using SC-CO$_2$ was first performed using the cubic array particle assembly (Fig. 5). The particle radius is 5 mm, and Young's modulus is 35.1 GPa. The two applied stresses are 10 MPa in the x direction and 12 MPa in the y direction. Other input parameters are the same as those in Table 2.

As shown in [14], the KGD solutions of fracture aperture (w) and fracture length (l) for the toughness-dominated regime are given as follows:

$$w(\xi, t) = 0.6828 \left(\frac{K'^2 Q t}{E'^2} \right)^{1/3} (1 - \xi^2)^{1/2} \quad (11)$$

$$l(t) = 0.9324 \left(\frac{E' Q t}{K'} \right)^{1/6} \quad (12)$$

where $\xi = x/l$ is the normalized coordinate along the fracture and x is the coordinate measured from the injection point.

The evolutions of fracture aperture and fracture length at $t = 0.9$ s in the numerical model and KGD model are compared in Fig. 6. Note that the input of mode I fracture toughness of the regular model was 1.88 Pa·m$^{1/2}$ in the KGD model in order to match numerical solution. The fracture length in the cubic array particle assembly is the distance between two fracture tips in the y direction. The fracture aperture at the injection point and the length in the KGD model are as follows: $w(0,0.9) = 7.52e{-}5$ m and $l(0.9) = 0.763$ m, while that calculated in the numerical model are $7.24e{-}5$ m and 0.770 m, respectively. The fracture width is underestimated by 3.9%, and the fracture length is overestimated by 1.1%. The small discrepancy can be attributed

Table 4 Summary of hydraulic fracturing simulation cases

Case ID	Fracturing fluid	S_{min}	S_{max}	Pre-existing fractures	Leak-off
Case 1-S1	100 cp fluid	10	12	No	No
Case 1-S2	100 cp fluid	10	15	No	No
Case 2-S1	SC-CO_2	10	12	No	No
Case 2-S2	SC-CO_2	10	15	No	No
Case N1-S1	100 cp fluid	10	12	Yes	No
Case N1-S2	100 cp fluid	10	15	Yes	No
Case N2-S1	SC-CO_2	10	12	Yes	No
Case N2-S2	SC-CO_2	10	15	Yes	No
Case L1-S1	100 cp fluid	10	12	No	Yes

to the gradual increase of rock modulus in the DEM modeling due to the opening of the fracture. Nevertheless, the results in Fig. 6 indicate that the numerical algorithm for the toughness-dominated regime is relatively accurate.

4 Numerical results

The cases of hydraulic fracturing with SC-CO_2 in the toughness-dominated regime and with 100 cp fracturing fluid approaching the viscosity-dominated regime were described and compared in this section. All cases were run with the random particle assembly to better mimic the rock materials.
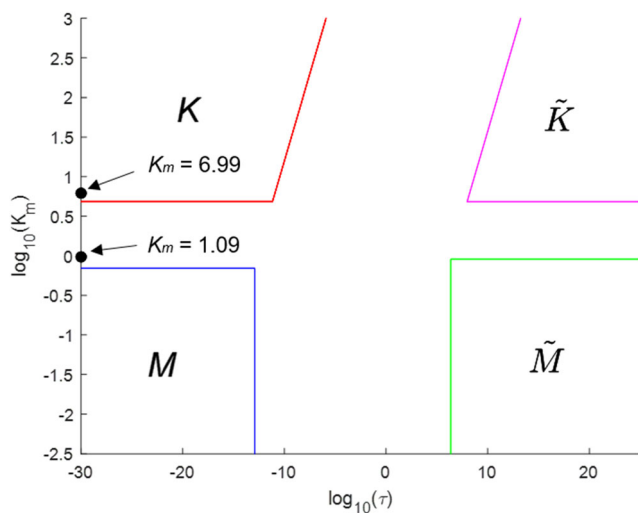
Fig. 4 The phase diagram of the fracture propagation regimes versus dimensionless time (τ) and toughness parameter (K_m) [14]. M, K, $\tilde{M}$, and $\tilde{K}$ represent the storage viscosity regime, the storage toughness regime, the leak-off viscosity regime, and the leak-off toughness regime, respectively. The black dots indicate the fracture propagation regimes with the input parameters in Table 2

4.1 Hydraulic fracturing in intact rock sample

In the cases of intact rock samples, the hydraulic fractures driven by the two types of fracturing fluid extend along the direction of maximum principal stress as shown in Fig. 7. The hydraulic fracture is tortuous, and the tortuosity can be used to evaluate fracture propagation pathways [27]. The tortuosity is defined as the total fracture length along a pathway (L_0) divided by the distance between the two ends of the fracture (L) in the reference area, and the total fracture length is calculated as the sum of the length of all microcracks generated in the model. When the stress difference is 2 MPa in case 1-S1 and case 2-S1, the results show that the tortuosity is 1.63 for SC-CO_2 and 1.19 for 100 cp fluid. The tendency in laboratory experiments using granite and shale is similar but with different values [26, 27, 29]. In the experiments using the granite [26, 27], the fractures induced by SC-CO_2 have a tortuosity up to 1.109, while those induced by oil ($\sim$320 cp) have a tortuosity up to 1.062. In the experiments using shale [29], the measured total fracture length contains branches, and the tortuosity is 5.602 for L-CO_2 and 1.090 for oil ($\sim$270 cp). The cases with larger stress difference show similar results. The calculated tortuosity suggests that SC-CO_2 has potential to generate more complex fracture networks and is desirable to enhance the hydrocarbon production in the field operations.

The net pressure and aperture along the hydraulic fractures are shown in Figs. 8 and 9. When comparing at the same injection fluid volume, hydraulic fracturing using more viscous fluid tends to induce a thicker and shorter fracture than that using SC-CO_2 in the toughness-dominated regime. The difference of fracture profiles can be explained by the distribution of fluid pressure in the fracture as shown in Figs. 8 a and 9 a. Uniform fluid pressure is applied throughout the SC-CO_2-induced fracture surface, while large-pressure gradient exists in the viscous fluid–induced fracture, and the closer it is to the tip, the greater the pressure gradient. The influence of fluid pressure distribution is analyzed in Section 5.
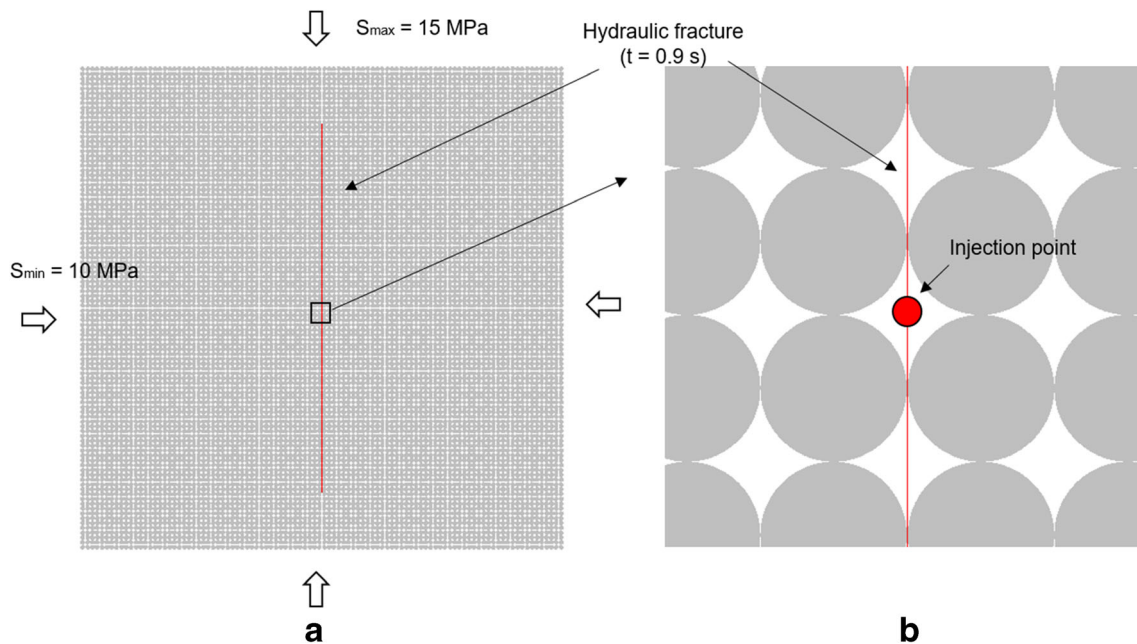
Fig. 5 **a** Schematic of the hydraulic fracturing verification model at $t = 0.9$ s. **b** Close-up view of the cubic array particle assembly

Evolution of injection fluid pressure and the tip location on the y-axis for the two types of fracturing fluid are compared in Figs. 10 and 11. The fracture length growth with a series of jumps is observed in the cases using SC-CO_2, and the jumps cause the immediate drop of the injection fluid pressure in the initial state. Moreover, the fracture induced by SC-CO_2 is more asymmetric as shown in Figs. 10 b and 11 b. The plateaus of the curve indicate that the fracture growth of one wing could be temporarily arrested due to the local inherent heterogeneity, which may shift the position of maximum aperture from the injection point (Fig. 11 b). By contrast, the hydraulic fracture driven by 100 cp fracturing fluid propagates more smoothly, continuously, and symmetrically over the flow

time. The results are in agreement with those observed in the hydraulic fracturing simulation in the toughness-dominated regime using the traditional hydromechanical coupling scheme [44]. During the fracturing process, the ratio between the particle size and the accumulated fracture length becomes smaller as the hydraulic fracture propagates, resulting in a stable injection fluid pressure with a decreasing fluctuation. Moreover, the propagation pressure for SC-CO_2 fracturing is much lower than that with high-viscosity fluid, and the former is slightly larger than the minimum principal stress (10 MPa). It is also observed that SC-CO_2 fracturing can reach a lower breakdown pressure (22.3 MPa for case 2-S1 and 22.1 MPa for case 2-S2) than the viscous fluid fracturing (24.1 MPa for
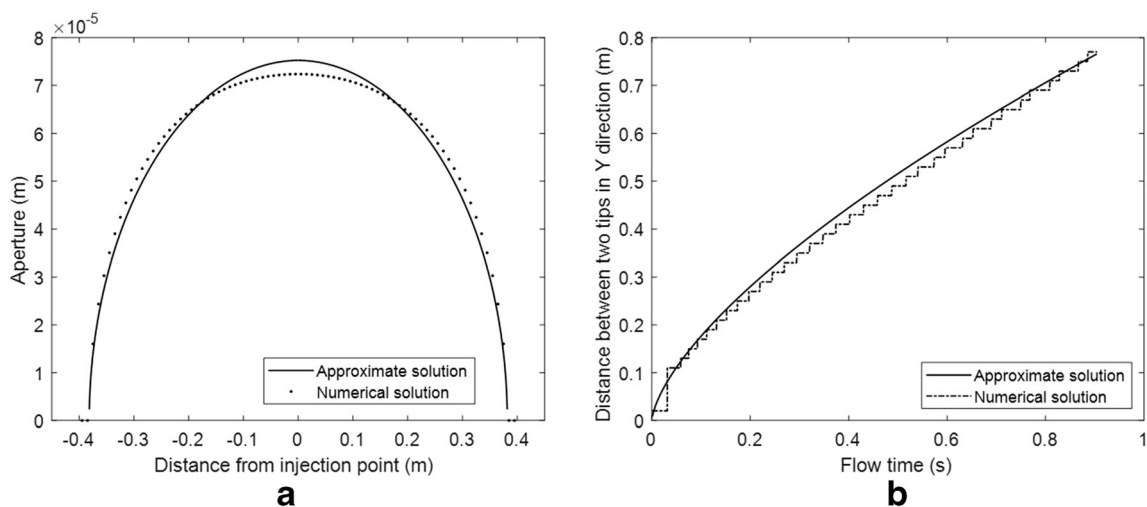

Fig. 6 Simulation results of hydraulic fracturing verification model with the cubic array particle assembly. **a** Comparison between the approximate solution and the numerical solution for fracture aperture. **b** Comparison between the approximate solution and the numerical solution for fracture length
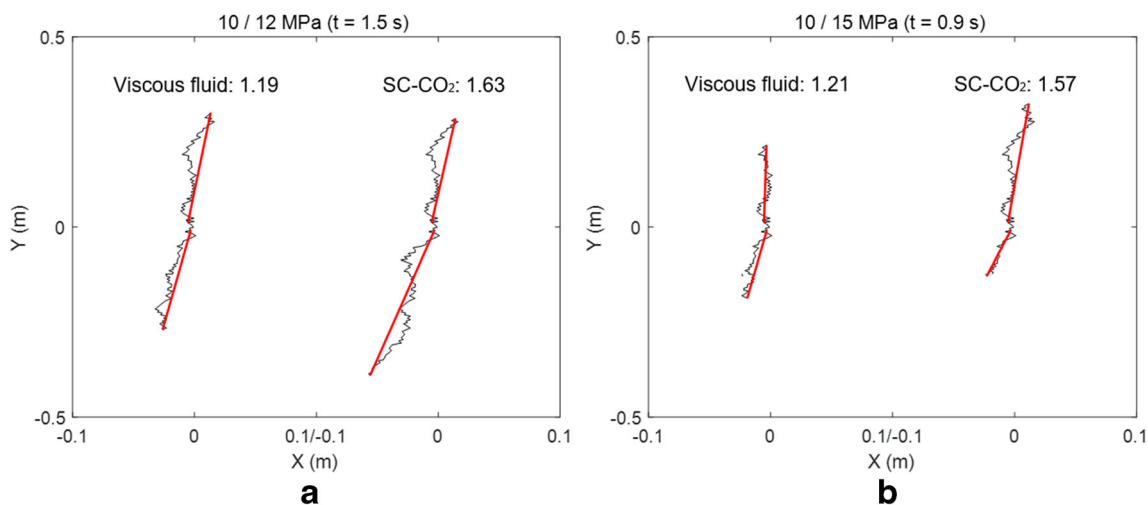
Fig. 7 Fracture profiles induced by 100 cp fracturing fluid and SC-CO$_2$, **a** in case 1-S1 and case 2-S1 at $t = 1.5$ s and **b** in case 1-S2 and case 2-S2 at $t = 0.9$ s. The black line represents the hydraulic fracture, and the red line shows the connection line of two ends. The numbers give the average tortuosity in the two directions for the fractures generated under different test conditions

case 1-S1 and 23.7 MPa for case 1-S2). However, the difference of breakdown pressure is less profound than that observed in previous experimental studies [25, 26]. The discrepancy may be attributed to the absence of circular borehole and fluid leak-off in this study, which is analyzed in Section 5.

The numerical results of case 2-S1 and the approximate solutions using the KGD model at $t = 1.5$ s are shown in Fig. 12. The fracture aperture at the injection point and the distance between two fracture tips in the y direction using the KGD model were $w(0, 1.5) = 10.40e{-}5$ m and $l(1.5) = 0.919$ m, while those calculated by the numerical model are $10.64e{-}5$ m and 0.683 m, respectively. The fracture aperture at the injection point is overestimated by 2.3%, while the distance between the two tips in the y direction is underestimated by 25.7%. It is obvious that there is a relatively large discrepancy, though the input of mode I

fracture toughness (2.66 Pa·m$^{1/2}$) is attempted to match the numerical solutions as well as possible. The apparent toughness (K_{IC}) scales with the tensile strength of the contact bond (σ_t') and the particle radius (R) as shown in [41, 45] is as follows: $K_{IC} \propto \sigma_t' \sqrt{R}$. However, due to the effect of internal heterogeneity, the mode I fracture toughness in case 2-S1 is larger than that in the regular model (1.88 Pa·m$^{1/2}$) regardless of the negative effect of decreasing the particle size. The possible explanation is that the fracture propagation in the toughness-dominated regime is more sensitive to the local inherent heterogeneity of the sample, resulting in less smooth fracture growth and more asymmetric and tortuous fractures as aforementioned. In real rock mass, the contact between particles might not be aligned with the direction of the maximum or minimum principal stresses, and the maximum horizontal stress may make some contribution to the con-
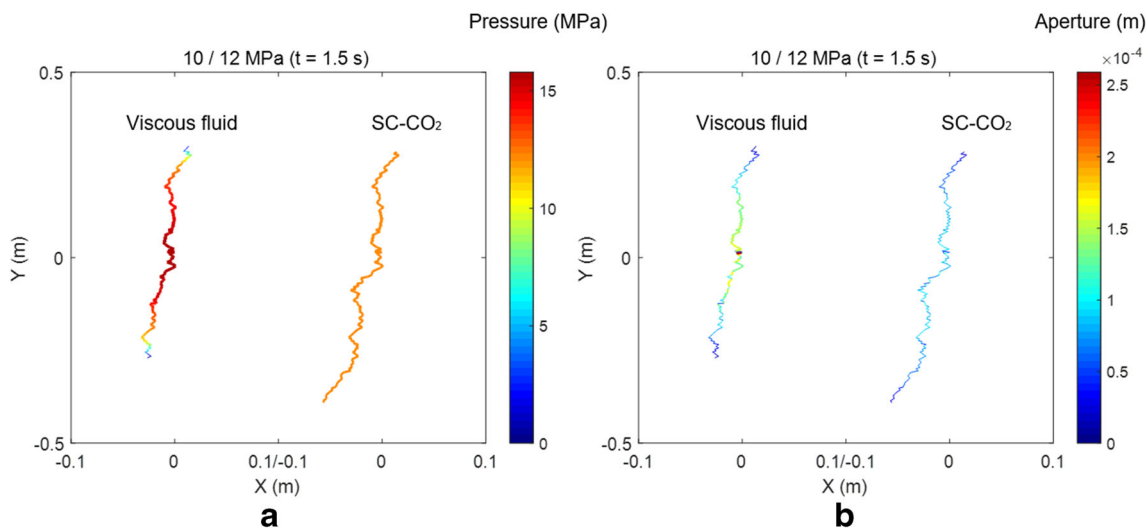

Fig. 8 **a** The net pressure of hydraulic fractures in case 1-S1 and case 2-S1 at $t = 1.5$ s. **b** The aperture of hydraulic fractures in case 1-S1 and case 2-S1 at $t = 1.5$ s. Both the color scale and the thickness of the lines indicate the net pressure in **a** and fracture width in **b**
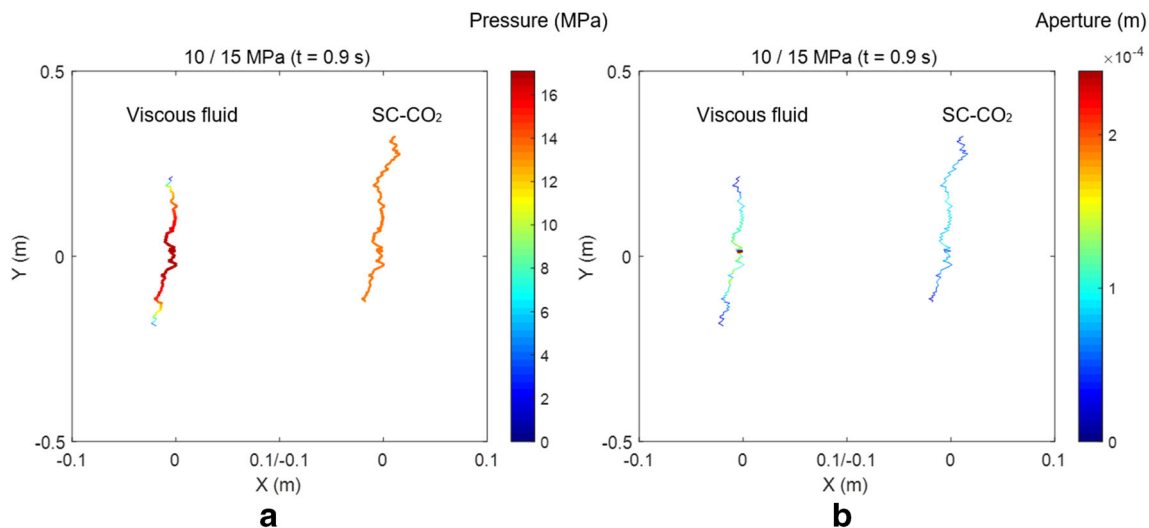
Fig. 9 **a** The net pressure of hydraulic fractures in case 1-S2 and case 2-S2 at $t = 0.9$ s. **b** The aperture of hydraulic fractures in case 1-S2 and case 2-S2 at $t = 0.9$ s. Both the color scale and the thickness of the lines indicate the net pressure in **a** and fracture width in **b**

tact force along the path of the hydraulic fracture. It is harder to fracture a random solid medium, and the hydraulic fracture propagation path is more tortuous. There is an increase of the effective toughness and a decrease of direct fracture length for the random model [44]. If the tortuosity is taken into consideration, the total accumulated fracture length is 1.099 m in case 2-S1. Thus, the fracture in the numerical solution is longer, thinner, and more tortuous than the one predicted by the KGD theoretical solution.

4.2 Hydraulic fracturing in fractured rock sample

It is widely accepted that rock mass contains pre-existing natural fractures and the propagation of hydraulic fracture could be greatly affected by those natural fractures or geological discontinuities [46–49]. As a fluid-driven fracture approaches the pre-existing fractures, the stress state around the fracture tip is disturbed, and this may cause complex fracture interaction

behavior [50–52]. In this study, four cases of hydraulic fracturing simulations were conducted to explore the fracture propagation behavior in rocks with pre-existing natural fractures.

Fig. 13 shows the evolution of injection fluid pressure using different fracturing fluids in the fractured rock sample for two horizontal stress differences. It is observed that the breakdown pressure and propagation pressure in SC-CO_2 fracturing are much lower compared to those in viscous fluid fracturing. This finding is similar to that observed in the intact rock sample. However, the pre-existing natural fractures cause the increase of breakdown pressure in the fractured rock sample compared to that in the intact rock sample. Note that the effect of natural fractures near wellbore on the breakdown pressure may be smaller in the real case because of the alternative path in the third dimension. Figs. 14 and 15 display the hydraulic fracture profiles when the injection volumes of the two fracturing fluid are the same. Fracture propagation deviates from the
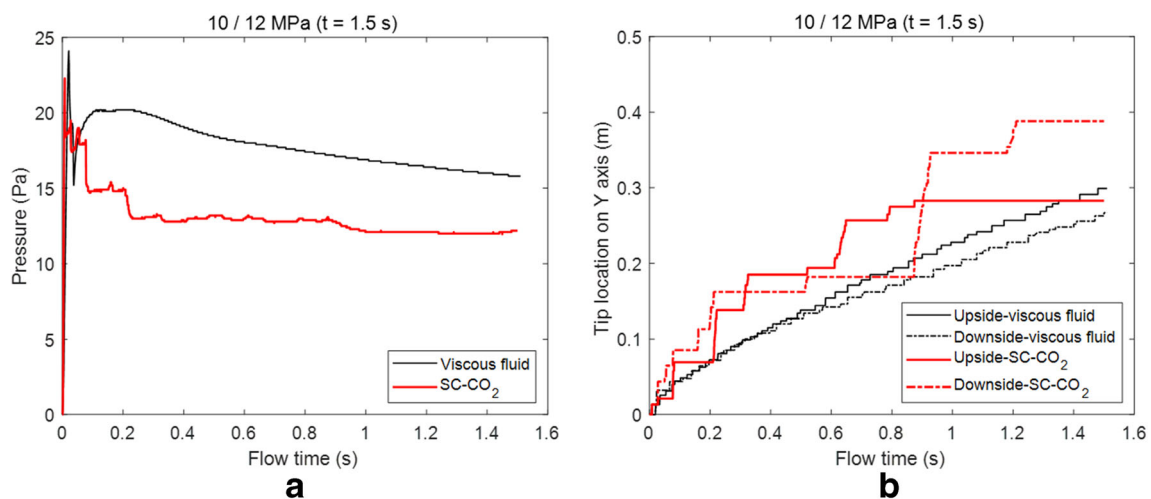

Fig. 10 **a** The history of injection fluid pressure in case 1-S1 and case 2-S1 at $t = 1.5$ s. **b** The evolution of tip location on the y-axis in case 1-S1 and case 2-S1 at $t = 1.5$ s
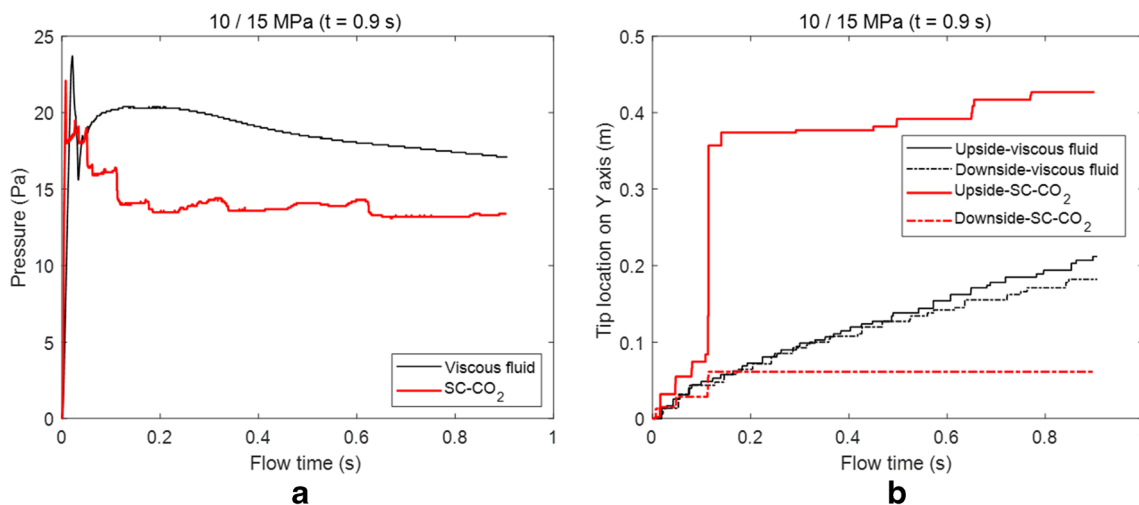
Fig. 11 **a** The history of injection fluid pressure in case 1-S2 and case 2-S2 at $t = 0.9$ s. **b** The evolution of tip location on the y-axis in case 1-S2 and case 2-S2 at $t = 0.9$ s

direction of the maximum confining stress through the interaction with natural fractures when the stress difference is low (see Fig. 14). When the stress difference is high, the hydraulic fracture induced by viscous fluid tends to propagate toward the pre-existing fractures. Once reaching the pre-existing fractures, the hydraulic fracture prefers to propagate along the pre-existing fractures as shown in Fig. 15 a. The asymmetric fractures driven by SC-CO_2 first propagate along the pre-existing natural fracture and then branch off and turn to the direction of the maximum confining stress (see Fig. 15 b).

It is obvious that SC-CO_2 induces a much longer fracture path. The number of accumulated microcracks is obtained to evaluate the ability to stimulate natural fractures as listed in Table 5. Compared with viscous fracturing fluid, more microcracks corresponding to the broken parallel bond are generated using SC-CO_2 at a low and high stress difference. When the stress difference is relatively high, SC-CO_2 fracturing

generates 168 microcracks in the pre-existing natural fractures, and 117 of them connect to the hydraulic fracture. However, in the case with viscous fluid, only 109 microcracks are generated and 57 of them connect to the hydraulic fracture. The results indicate that SC-CO_2 fracturing tends to achieve a more complex and productive fracture network than fracturing with high-viscosity fluid. The results are consistent with the findings in the laboratory experiments [28, 33].

5 Discussion

5.1 Breakdown pressure

A fluid-driven fracture in rock usually propagates in mode I [7]. In the case of a two-dimensional fracture in an infinite plane as shown in Fig. 16 a, the stress intensity factor at the
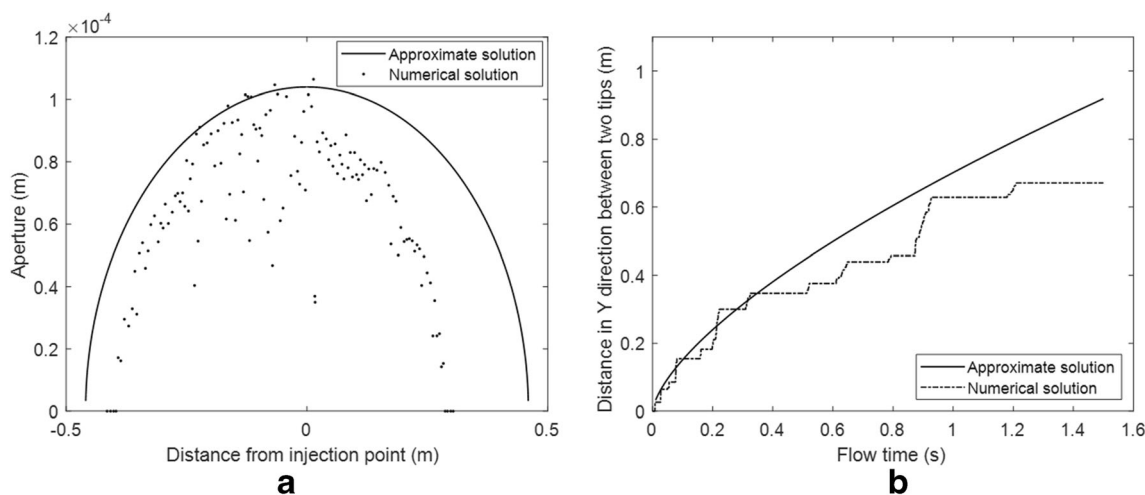

Fig. 12 Simulation results of hydraulic fracturing for random models. **a** Comparison between the approximate solution and the numerical solution for hydraulic fracture aperture. **b** Comparison between the approximate solution and the numerical solution for the distance in the y direction between two fracture tips
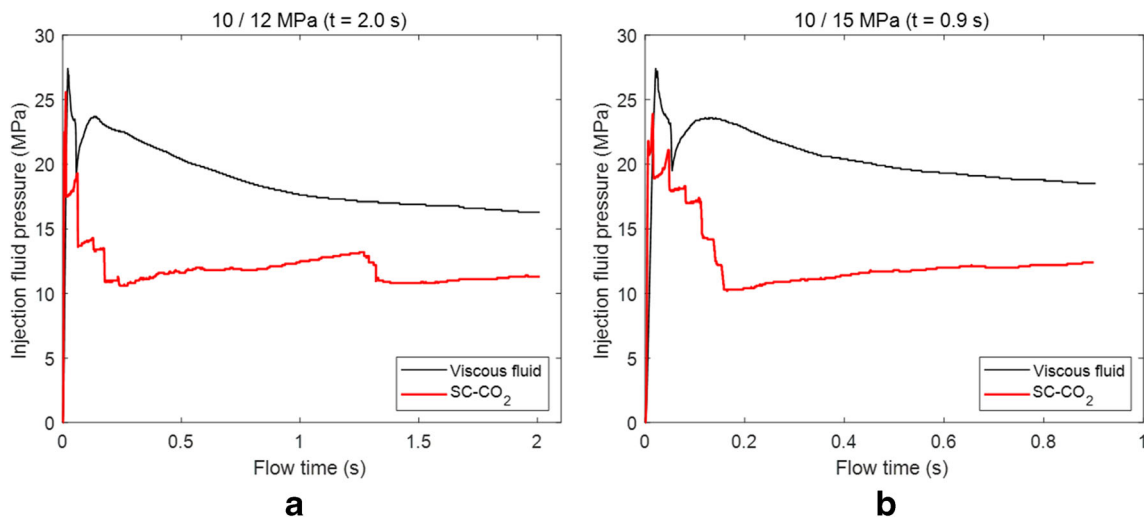
Fig. 13 The history of injection fluid pressure of **a** case N1-S1 and case N2-S1 and **b** case N1-S2 and case N2-S2

fracture tip is as follows [53]:

$$K_{\mathrm{I}} = \frac{\sqrt{2l}}{\sqrt{\pi}} \int_{0}^{\frac{1}{2}l} \frac{p(\xi)}{\sqrt{\frac{1}{4}l^2 - \xi^2}} d\xi \tag{13}$$

where $p(\xi)$ is the pressure applied on the fracture surface and l is the fracture length. The fracture propagates once the mode I stress intensity factor at the fracture tip is equal to the fracture toughness.

In two particular cases, case 1 with a pair of point loads (F) was applied to the fracture (see Fig. 16b) and case 2 with the uniform pressure load (p) acting throughout the whole fracture (see Fig. 16c) [54]. Then, Eq. (13) can be simplified into the following two expressions:

$$K_{\mathrm{I}} = \frac{F}{\sqrt{\frac{1}{2}\pi l}} \tag{14}$$

$$K_{\mathrm{I}} = p\sqrt{\frac{1}{2}\pi l} \tag{15}$$

For the modeling in this study, there are three preset microcracks acting as a borehole. The fluid pressure acts on the fracture uniformly with a finite length (l), which is the distance between the two fracture tips. As shown in Fig. 1 a, the length of a microcrack is the distance between the two active domains, and the fracture tip is not in the domain center but in the contact point. Thus, the finite length is about 4 times the particle diameter, much smaller than the size of the rock
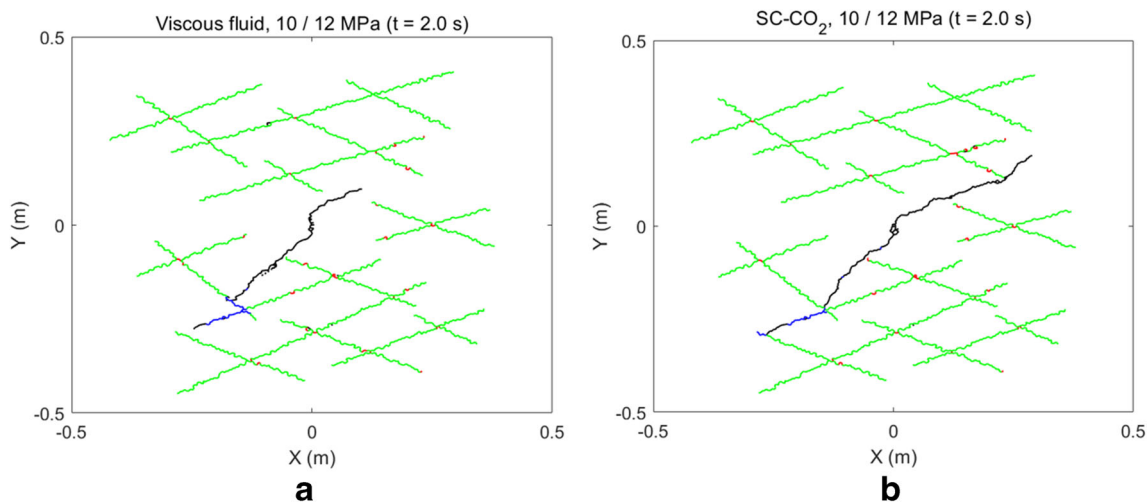

Fig. 14 Fracture profiles at $t = 2.0$ s. **a** Case N1-S1. **b** Case N2-S1. The black and green lines represent the hydraulic fracture and the pre-existing fracture, respectively. The blue and red lines indicate the active

microcracks (in pre-existing fractures) connecting and disconnecting to the hydraulic fracture, respectively
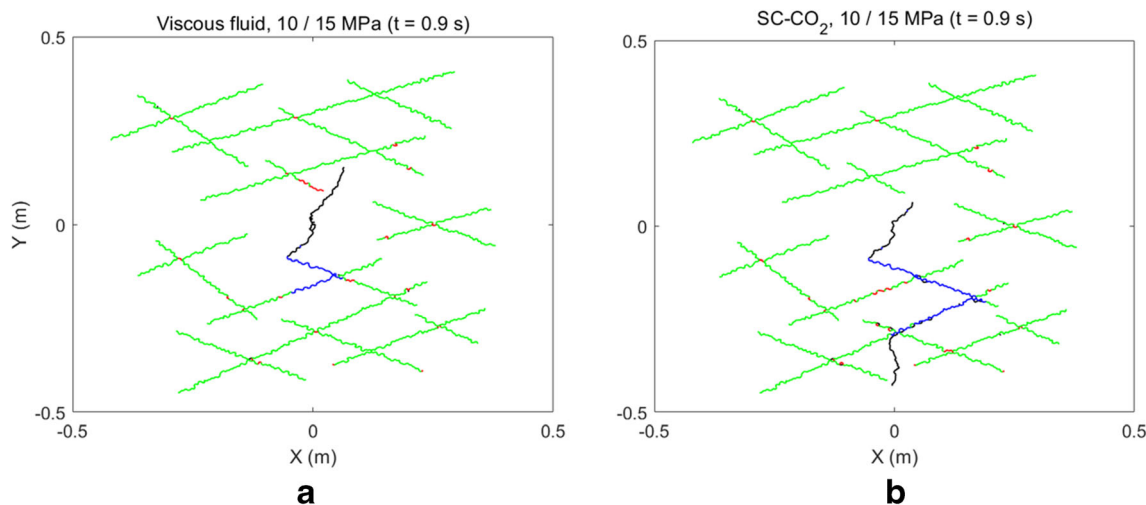
Fig. 15 Fracture profiles at $t = 0.9$ s. **a** Case N1-S2. **b** Case N2-S2

sample. Therefore, when the fracture toughness and the finite length are respectively $K_{IC} = 2.66$ Pa·m$^{1/2}$ and $l = 0.032$ m, the back-calculated pressure is 11.9 MPa based on Eq. (15). Taking the minimum principal pressure (10 MPa) into consideration, the estimated injection pressure is about 21.9 MPa when the fracture initiates. Then, the breakdown pressure is 21.9 MPa or larger, since the fracture initiation could occur before the breakdown [19]. The above results for the breakdown pressure are consistent with the numerical results. Besides, because of the absence of a circular borehole, the effect of stress difference on the breakdown pressure is minimized. The existence of preset fracture with a finite length accounts for the small difference in the breakdown pressure in these four cases (case 1-S1, case 1-S2, case 2-S1, and case 2-S2).

To investigate the influence of fluid leak-off, an additional viscous fluid fracturing case (case L1-S1) considering fluid leak-off with a low stress difference was carried out, and a comparison with zero fluid leak-off case (case 1-S1) was made. The simulation parameters of case L1-S1 are the same as those of case 1-S1 except that the fluid flow into the rock matrix is turned on in case L1-S1. The injection fluid pressure and fracture length with respect to flow time are shown in

Fig. 17 a. The breakdown pressure in case L1-S1 and case 1-S1 is 21.0 MPa and 24.1 MPa, respectively. There is a decrease of breakdown pressure if the fluid leak-off is involved. The fluid infiltration before fracture initiation causes an additional pore pressure around the borehole [35, 37] (see Fig. 17 b). The pore pressure reduces the effective stress and effective toughness around the borehole, resulting in a lower initiation pressure. However, the additional energy dissipation due to the viscous fluid infiltration leads to a higher fracture propagation pressure after the breakdown. It is noted that the additional energy dissipation by fluid infiltration could become less significant if a smaller fluid viscosity is applied.

5.2 Fracture propagation process

The fluid pressure acting on the fracture surface varies depending on the regimes of hydraulic fracture propagation [13, 14]. The fracture propagations in the viscosity-dominated regime and the toughness-dominated regime are in a state close to Fig. 16 b and c, respectively [26]. Fig. 18 displays the minimum principal stress contour after the hydraulic fracture propagation in case 1-S1 and case 2-S1. The black line represents the traces of the hydraulic fracture.

Table 5 Accumulated numbers of microcracks in the fractured rock samples

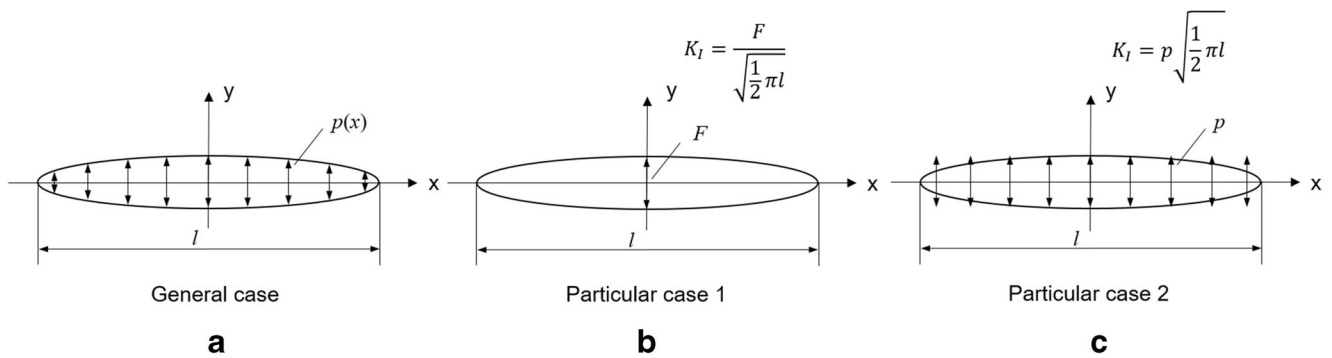| Numbers of microcracks	10/12 MPa ($t = 2.0$ s)	10/15 MPa ($t = 0.9$ s)		
	Case N1-S1	Case N2-S1	Case N1-S2	Case N2-S2
Broken parallel bonds	104	154	62	87
Broken smooth joints connecting to the main fracture	41	32	57	117
Broken smooth joints disconnecting to the main fracture	51	55	52	51
Broken smooth joints	92	87	109	168
Total	196	241	171	255

Fig. 16 Fracture growth from a viewpoint of mode I stress intensity factor at the fracture tip under **a** distributed load, **b** point load, and **c** uniform load

Case 1-S1 using viscous fluid shows a much larger variation of stress from the injection point to the tip than case 2-S1 with SC-CO$_2$ due to the difference of pressure distribution inside the fracture. With the uniform fluid pressure in the fracture for case 2-S1, the information of injection point and the ability to guide the geometrical evolution of the fracture tip could be lost. Besides, the fracture growth in the toughness-dominated regime is more sensitive to the inherent heterogeneity of rock [44]. Thus, the fracture propagation direction in case 2-S1 is more variable, resulting in larger fracture tortuosity and asymmetry. It should be noted that the simulation cases are performed in two-dimensional in this study. In reality, the more alternative paths in the third dimension have a more significant impact on the fracture profiles when using different fracturing fluids, and SC-CO$_2$ has potential to generate more complex fracture networks.

Based on Eq. (15), K_I increases with the fracture length (l) if the injection pressure (p) is fixed. In reality, the injection fluid pressure decreases once the K_I at the fracture tip is equal to K_{IC} and the fracture tip extends. After each fracture extension, the pressure in the fracture needs to accumulate again before the next extension. Thus, the

fracture growth induced by low-viscosity fluid like SC-CO$_2$ is less smooth and continuous with a series of jumps as observed in Figs. 10 and 11.

5.3 Effect of fluid compressibility

SC-CO$_2$ has higher compressibility than traditional hydraulic fracturing fluids such as slick water. The relationship between SC-CO$_2$ density and pressure is almost linear for the value greater than 35 MPa when the temperature is constant [55–57]. Based on the assumption of linear-compressibility law, Wang et al. [56, 57] found that the compressibility affects fracture growth only at the very beginning period in the storage-dominated regime (M and K in Fig. 4), and a slightly greater fracture length is observed due to the fluid expansion. Besides, the influence of fluid compressibility can be neglected in the permeable rock when the fluid leak-off dominates ($\widetilde{M}$ and $\widetilde{K}$ in Fig. 4). The numerical study by Zhou and Burbey [34] indicated that the effect of fluid viscosity can dominate and mask the effect of fluid compressibility. Therefore, the compressibility of SC-CO$_2$ is the minor factor
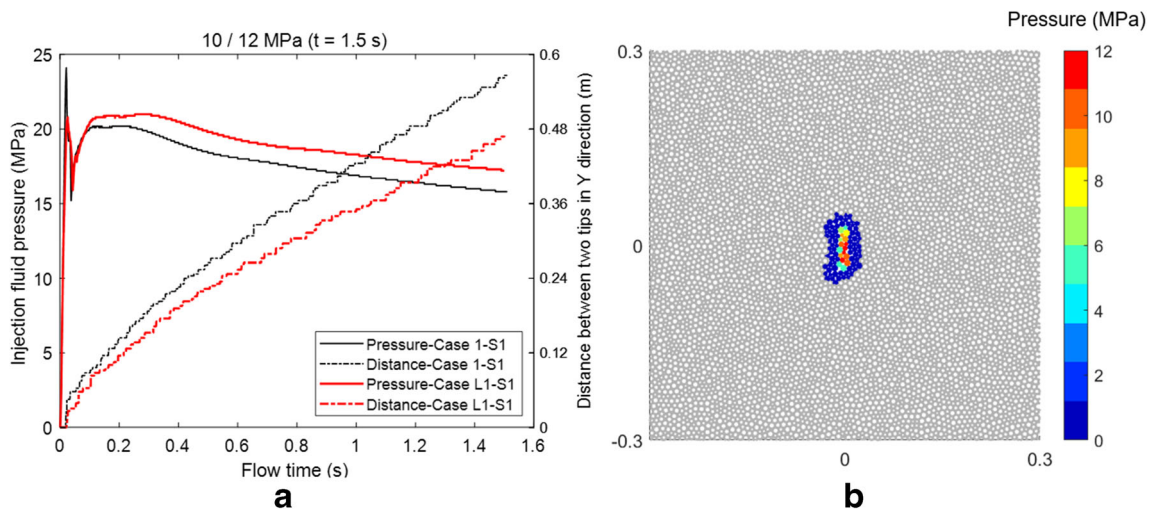

Fig. 17 **a** The history of injection pressure and the distance between two tips in the y direction in case 1-S1 and case L1-S1 at $t = 1.5$ s. **b** The distribution of pore pressure before fracture initiation. The gray hollow

circles represent particles with dry pore space, and the filled circles show those with saturated pore spaces. The filled color indicates the magnitude of the locally averaged pore pressure at the positions of particles
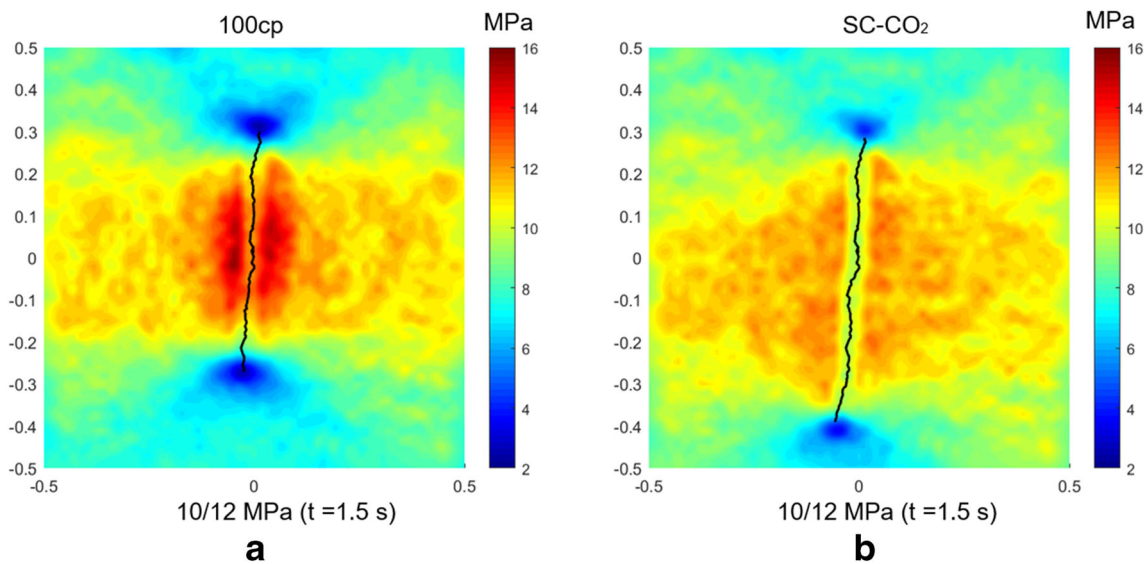
Fig. 18 The minimum principal stress contour after the hydraulic fracture propagation in **a** case 1-S1 and **b** case 2-S1. The black line represents the traces of the hydraulic fracture

and it is valid that the compressibility is not considered in this study.

6 Conclusions

In this study, a new DEM-based numerical algorithm is developed to investigate the micromechanical behavior of SC-CO$_2$ fracturing in both intact and fractured rock samples, and hydraulic fracturing cases using 100 cp fracturing fluid are also performed for comparison. In the toughness-dominated regime, the pressure gradient inside the fracture can be ignored and the pressure is treated as uniform. The new algorithm shows high accuracy based on a comparison with the reference solution for a plane strain KGD hydraulic fracture. Moreover, it has much higher computational efficiency, which is more than 100 times than the traditional hydromechanical scheme for hydraulic fracturing with low fluid viscosity. The following conclusions can be drawn from this numerical study.

1. The hydraulic fracture propagation in intact rock driven by SC-CO$_2$ in the toughness-dominated regime tends to be less smooth and continuous, more asymmetric, and tortuous than that driven by high-viscosity fluid.
2. The fluid pressure acting on the fracture surface varies for the high- and low-viscosity fracturing fluids. The fluid pressure in the whole fracture driven by SC-CO$_2$ is uniform, while large pressure gradient exists in the fracture induced by viscous fluid.
3. In the cases using SC-CO$_2$, the uniform pressure inside the fracture causes a much smaller variation of stress and makes the information of injection point and the ability to

guide the geometrical evolution of the fracture tip lost. Therefore, the fracture propagation direction is more variable in SC-CO$_2$ fracturing, resulting in a more tortuous and asymmetric fracture path.

4. For SC-CO$_2$ fracturing, the injection fluid pressure decreases once the K_I at the fracture tip is equal to K_{IC} and the fracture tip extends. After each fracture extension, the pressure in the fracture needs to accumulate again before the next extension. Thus, the fracture growth induced by low-viscosity fluid like SC-CO$_2$ is less smooth and continuous.
5. The breakdown pressure increases with the viscosity of fracturing fluid. The difference of breakdown pressure is less profound in this study. The existence of the preset fracture with a finite length eases the influence of principal stress and fluid viscosity. In reality, the low-viscosity fluid like SC-CO$_2$ can lead to a much lower breakdown pressure with the circular borehole and the fluid leak-off involved.
6. In the fractured rock mass, the fracture propagation could deviate from the direction of the maximum confining stress under the low stress difference. Compared with viscous fluid, SC-CO$_2$ tends to cause a more complex fracture network with a longer main fracture in the rock matrix and more activated microcracks in the pre-existing natural fractures.
7. The fluid infiltration before fracture initiation could reduce the effective stress and the effective toughness around the borehole, resulting in a lower initiation pressure. However, the additional energy dissipation due to viscous fluid infiltration could lead to a higher fracture propagation pressure after the breakdown.

It is also worth mentioning that there are some limitations in this study and future work is required. The influence of leak-off on the breakdown pressure and propagation pressure is discussed using viscous fluid in this study. For further investigation on the fluid infiltration of SC-CO$_2$, the improvement of the new algorithm for the toughness-dominated regime is required. The high injection rate and low viscosity of SC-CO$_2$ can lead to high Reynolds numbers and potential turbulence in the fracture [58], which could be considered in the future work.

References

1. Middleton, R.S., Carey, J.W., Currier, R.P., Hyman, J.D., Kang, Q., Karra, S., Jiménez-Martínez, J., Porter, M.L., Viswanathan, H.S.: Shale gas and non-aqueous fracturing fluids: opportunities and challenges for supercritical CO$_2$. Appl. Energy. **147**, 500–509 (2015). https://doi.org/10.1016/j.apenergy.2015.03.023

2. Annevelink, M.P.J.A., Meesters, J.A.J., Hendriks, A.J.: Environmental contamination due to shale gas development. Sci. Total Environ. **550**, 431–438 (2016). https://doi.org/10.1016/j.scitotenv.2016.01.131

3. Sampath, K.H.S.M., Perera, M.S.A., Ranjith, P.G., Matthai, S.K., Rathnaweera, T., Zhang, G., Tao, X.: CH$_4$–CO$_2$ gas exchange and supercritical CO$_2$ based hydraulic fracturing as CBM production-accelerating techniques: a review. J. CO$_2$ Util. **22**(212–230), (2017). https://doi.org/10.1016/j.jcou.2017.10.004

4. Zhang, C., Gamage, R.P., Perera, M.S.A., Zhao, J.: Characteristics of clay-abundant shale formations: use of CO$_2$ for production enhancement. Energies. **10**, 5–7 (2017). https://doi.org/10.3390/en10111887

5. Gensterblum, Y., Busch, A., Krooss, B.M.: Molecular concept and experimental evidence of competitive adsorption of H$_2$O, CO$_2$ and CH$_4$ on organic material. Fuel. **115**, 581–588 (2014). https://doi.org/10.1016/j.fuel.2013.07.014

6. Soltanian, M.R., Dai, Z.: Geologic CO$_2$ sequestration: progress and challenges. Geomech. Geophys. Geo-Energy Geo-Resources. **3**, 221–223 (2017). https://doi.org/10.1007/s40948-017-0066-2

7. Detournay, E.: Mechanics of hydraulic fractures. Annu. Rev. Fluid Mech. **48**, 311–339 (2016). https://doi.org/10.1146/annurev-fluid-010814-014736

8. Savitski, A.A., Detournay, E.: Propagation of a penny-shaped fluid-driven fracture in an impermeable rock: asymptotic solutions. Int. J. Solids Struct. **39**, 6311–6337 (2002). https://doi.org/10.1016/S0020-7683(02)00492-4

9. Garagash, D.I.: Plane-strain propagation of a fluid-driven fracture during injection and shut-in: asymptotics of large toughness. Eng. Fract. Mech. **73**, 456–481 (2006). https://doi.org/10.1016/j.engfracmech.2005.07.012

10. Adachi, J.I., Detournay, E.: Plane strain propagation of a hydraulic fracture in a permeable rock. Eng. Fract. Mech. **75**, 4666–4694 (2008). https://doi.org/10.1016/j.engfracmech.2008.04.006

11. Bunger, A.P., Detournay, E., Garagash, D.I.: Toughness-dominated hydraulic fracture with leak-off. Int. J. Fract. **134**, 175–190 (2005). https://doi.org/10.1007/s10704-005-0154-0

12. Fenghour, A., Wakeham, W.A.: The viscosity of carbon dioxide. J. Phys. Chem. Ref. Data. **27**, 31–44 (1998). https://doi.org/10.1063/1.556013

13. Hu, J., Garagash, D.I.: Plane-strain propagation of a fluid-driven crack in a permeable rock with fracture toughness. J. Eng. Mech. **136**, 1152–1166 (2010). https://doi.org/10.1061/(ASCE)EM.1943-7889.0000169

14. Dontsov, E.V.: An approximate solution for a plane strain hydraulic fracture that accounts for fracture toughness, fluid viscosity, and leak-off. Int. J. Fract. **205**, 221–237 (2017). https://doi.org/10.1007/s10704-017-0192-4

15. Dontsov, E.V.: An approximate solution for a penny-shaped hydraulic fracture that accounts for fracture toughness, fluid viscosity and leak-off. R. Soc. Open Sci. **3**, 160737 (2016). https://doi.org/10.1098/rsos.160737

16. Hubbert, M.K., Willis, D.G.: Mechanics of hydraulic fracturing. Soc. Pet. Eng. **210**, 153–168 (1957)

17. Haimson, B.C., Fairhurst, C.: Initiation and extension of hydraulic fractures in rocks. Soc. Pet. Eng. J. **7**, 310–318 (1967)

18. Haimson, B.C., Fairhurst, C.: Hydraulic fracturing in porous-permeable materials. J. Pet. Technol. **21**, 811–817 (1969). https://doi.org/10.1515/FREQ.1998.52.3-4.54

19. Zoback, M.D., Rummel, F., Jung, R., Raleigh, C.B.: Laboratory hydraulic fracturing experiments in intact and pre-fractured rock. Int. J. Rock Mech. Min. Sci. **14**, 49–58 (1977). https://doi.org/10.1016/0148-9062(77)90196-6

20. Garagash, D., Detournay, E.: An analysis of the influence of the pressurization rate on the borehole breakdown pressure. Int. J. Solids Struct. **34**, 3099–3118 (1997). https://doi.org/10.1016/S0020-7683(96)00174-6

21. Zhao, L., Qin, X., Zhang, J., Liu, X., Han, D. Hua, Geng, J., Xiong, Y.: An effective reservoir parameter for seismic characterization of organic shale reservoir. Springer Netherlands (2018)

22. Gan, Q., Elsworth, D., Alpern, J.S., Marone, C., Connolly, P.: Breakdown pressures due to infiltration and exclusion in finite length boreholes. J. Pet. Sci. Eng. **127**, 329–337 (2015). https://doi.org/10.1016/j.petrol.2015.01.011

23. Alpern, J.S., Marone, C.J., Elsworth, D., Belmonte, A., Connelly, P.: Exploring the physicochemical processes that govern hydraulic fracture through laboratory experiments. In: 46th U.S. Rock Mechanics/Geomechanics Symposium, Chicago, IL, USA. (2012)

24. Ishida, T., Chen, Q., Mizuta, Y., Roegiers, J.-C.: Influence of fluid viscosity on the hydraulic fracturing mechanism. J. Energy Resour. Technol. **126**, 190–200 (2004). https://doi.org/10.1115/1.1791651

25. Ishida, T., Aoyagi, K., Niwa, T., Chen, Y., Murata, S., Chen, Q., Nakayama, Y.: Acoustic emission monitoring of hydraulic fracturing laboratory experiment with supercritical and liquid CO$_2$. Geophys. Res. Lett. **39**, L16309 (2012). https://doi.org/10.1029/2012GL052788

26. Ishida, T., Chen, Y., Bennour, Z., Yamashita, H., Inui, S., Nagaya, Y., Naoi, M., Chen, Q., Nakayama, Y., Nagano, Y.: Features of CO$_2$ fracturing deduced from acoustic emission and microscopy in laboratory experiments. J. Geophys. Res. Solid Earth. **121**, 8080–8098 (2016). https://doi.org/10.1002/2016JB013365

27. Chen, Y., Nagaya, Y., Ishida, T.: Observations of fractures induced by hydraulic fracturing in anisotropic granite. Rock Mech. Rock. Eng. **48**, 1455–1461 (2015). https://doi.org/10.1007/s00603-015-0727-9

28. Zhang, X., Lu, Y., Tang, J., Zhou, Z., Liao, Y.: Experimental study on fracture initiation and propagation in shale using supercritical

carbon dioxide fracturing. Fuel. **190**, 370–378 (2017). https://doi.org/10.1016/j.fuel.2016.10.120

29. Bennour, Z., Watanabe, S., Chen, Y., Ishida, T., Akai, T.: Evaluation of stimulated reservoir volume in laboratory hydraulic fracturing with oil, water and liquid carbon dioxide under microscopy using the fluorescence method. Geomech. Geophys. Geo-Energy Geo-Resources. **4**, 39–50 (2018). https://doi.org/10.1007/s40948-017-0073-3

30. Weng, X.: Modeling of complex hydraulic fractures in naturally fractured formation. J. Unconv. Oil Gas Resour. **9**, 114–135 (2015). https://doi.org/10.1016/j.juogr.2014.07.001

31. Bennour, Z., Ishida, T., Nagaya, Y., Chen, Y., Nara, Y., Chen, Q., Sekine, K., Nagano, Y.: Crack extension in hydraulic fracturing of shale cores using viscous oil, water, and liquid carbon dioxide. Rock Mech. Rock. Eng. **48**, 1463–1473 (2015). https://doi.org/10.1007/s00603-015-0774-2

32. Song, X., Guo, Y., Zhang, J., Sun, N., Shen, G., Chang, X., Yu, W., Tang, Z., Chen, W., Wei, W., Wang, L., Zhou, J., Li, X., Li, X., Zhou, J., Xue, Z.: Fracturing with carbon dioxide: from microscopic mechanism to reservoir application. Joule. **3**, 1913–1926, 1–14 (2019). https://doi.org/10.1016/j.joule.2019.05.004

33. Zou, Y., Li, N., Ma, X., Zhang, S., Li, S.: Experimental study on the growth behavior of supercritical CO_2-induced fractures in a layered tight sandstone formation. J. Nat. Gas Sci. Eng. **49**, 145–156 (2018). https://doi.org/10.1016/j.jngse.2017.11.005

34. Zhou, X., Burbey, T.J.: Fluid effect on hydraulic fracture propagation behavior: a comparison between water and supercritical CO_2-like fluid. Geofluids. **14**, 174–188 (2014). https://doi.org/10.1111/gfl.12061

35. Shimizu, H., Murata, S., Ishida, T.: The distinct element analysis for hydraulic fracturing in hard rock considering fluid viscosity and particle size distribution. Int. J. Rock Mech. Min. Sci. **48**, 712–727 (2011). https://doi.org/10.1016/j.ijrmms.2011.04.013

36. Zhang, X., Wang, J.G., Gao, F., Ju, Y.: Impact of water, nitrogen and CO_2 fracturing fluids on fracturing initiation pressure and flow pattern in anisotropic shale reservoirs. J. Nat. Gas Sci. Eng. **45**, 291–306 (2017). https://doi.org/10.1016/j.jngse.2017.06.002

37. Wang, J., Elsworth, D., Wu, Y., Liu, J., Zhu, W., Liu, Y.: The influence of fracturing fluids on fracturing processes: a comparison between water, oil and SC-CO_2. Rock Mech. Rock. Eng. **51**, 299–313 (2018). https://doi.org/10.1007/s00603-017-1326-8

38. Peng, P., Ju, Y., Wang, Y., Wang, S., Gao, F.: Numerical analysis of the effect of natural microcracks on the supercritical CO_2 fracturing crack network of shale rock based on bonded particle models. Int. J. Numer. Anal. Methods Geomech. **41**, 1992–2013 (2017). https://doi.org/10.1002/nag.2712

39. Itasca Consulting Group: PFC2D—particle flow code in 2 dimensions, version 5.0. Minneapolis, Minnesota, USA (2014)

40. Cundall, P.A., Strack, O.D.L.: A discrete numerical model for granular assemblies. Géotechnique. **29**, 47–65 (1979). https://doi.org/10.1680/geot.1979.29.1.47

41. Potyondy, D.O., Cundall, P.A.: A bonded-particle model for rock. Int. J. Rock Mech. Min. Sci. **41**, 1329–1364 (2004). https://doi.org/10.1016/j.ijrmms.2004.09.011

42. Mas Ivars, D., Pierce, M.E., Darcel, C., Reyes-Montes, J., Potyondy, D.O., Paul Young, R., Cundall, P.A.: The synthetic rock mass approach for jointed rock mass modelling. Int. J. Rock Mech. Min. Sci. **48**, 219–244 (2011). https://doi.org/10.1016/j.ijrmms.2010.11.014

43. Zhang, F., Damjanac, B., Huang, H.: Coupled discrete element modeling of fluid injection into dense granular media. J. Geophys. Res. Solid Earth. **118**, 2703–2722 (2013). https://doi.org/10.1002/jgrb.50204

44. Huang, L., Liu, J., Zhang, F., Dontsov, E., Damjanac, B.: Exploring the influence of rock inherent heterogeneity and grain size on hydraulic fracturing using discrete element modeling. Int. J. Solids Struct. (2019). https://doi.org/10.1016/j.ijsolstr.2019.06.018

45. Huang, H.: Discrete element modeling of tool-rock interaction. University of Minnesota, Minneapolis (1999)

46. Zhang, F., Damjanac, B., Maxwell, S.: Investigating hydraulic fracturing complexity in naturally fractured rock masses using fully coupled multiscale numerical modeling. Rock Mech. Rock. Eng. (2019). https://doi.org/10.1007/s00603-019-01851-3

47. Hou, B., Chang, Z., Fu, W., Muhadasi, Y., Chen, M.: Fracture initiation and propagation in a deep shale gas reservoir subject to an alternating-fluid-injection hydraulic-fracturing treatment. SPE J. **24**, 1–17 (2019). https://doi.org/10.2118/195571-pa

48. Zhao, L., Qin, X., Han, D.H., Geng, J., Yang, Z., Cao, H.: Rock-physics modeling for the elastic properties of organic shale at different maturity stages. Geophysics. **81**, D527–D541 (2016). https://doi.org/10.1190/GEO2015-0713.1

49. Zhang, F., Yin, Z., Chen, Z., Maxwell, S., Zhu, H., Zhang, L., Wu, Y.: Fault reactivation and induced seismicity during multi-stage hydraulic fracturing: microseismic analysis and geomechanical modeling. SPE J. In print. (2019). https://doi.org/10.2118/199883-PA

50. Renshaw, C.E., Pollard, D.D.: An experimentally verified criterion for propagation across unbounded frictional interfaces in brittle, linear elastic materials. Int. J. Rock Mech. Min. Sci. **32**, 237–249 (1995). https://doi.org/10.1016/0148-9062(94)00037-4

51. Zhang, F., Dontsov, E., Mack, M.: Fully coupled simulation of a hydraulic fracture interacting with natural fractures with a hybrid discrete-continuum method. Int. J. Numer. Anal. Methods Geomech. **41**, 1430–1452 (2017). https://doi.org/10.1002/nag.2682

52. Tang, J., Wu, K., Zuo, L., Xiao, L., Sun, S., Ehlig-Economides, C.: Investigation of rupture and slip mechanisms of hydraulic fracture in multiple-layered formations. Soc. Pet. Eng. J. (2019). https://doi.org/10.2118/197054-PA

53. Tada, H., Paris, P.C., Irwin, G.R.: The stress analysis of crack handbook, (2000)

54. Zoback, M.D., Pollard, D.D.: Hydraulic fracture propagation and the interpretation of pressure-time records for in-situ stress determination. In: Proceedings of 19th US Rock Mechanics Symposium. pp. 14–22. Reno, Nev (1978)

55. Span, R., Wagner, W.: A new equation of state for carbon dioxide covering the fluid region from the triple-point temperature to 1100 K at pressures up to 800 MPa. J. Phys. Chem. Ref. Data. **25**, 1509–1596 (1996). https://doi.org/10.1063/1.555991

56. Wang, D., Chen, M., Jin, Y., Bunger, A.P.: Effect of fluid compressibility on toughness-dominated hydraulic fractures with leakoff. SPE J. **23**, 2118–2132 (2018). https://doi.org/10.2118/193995-pa

57. Wang, D., Chen, M., Jin, Y., Bunger, A.P.: Impact of fluid compressibility for plane strain hydraulic fractures. Comput. Geotech. **97**, 20–26 (2018). https://doi.org/10.1016/j.compgeo.2017.12.009

58. Zia, H., Lecampion, B.: Propagation of a height contained hydraulic fracture in turbulent flow regimes. Int. J. Solids Struct. **110–111**, 265–278 (2017). https://doi.org/10.1016/j.ijsolstr.2016.12.029